minerals

Article

Multi-Scale Potential Field Data Integration Using Fuzzy C-Means Clustering for Automated Geological Mapping of North Singhbhum Mobile Belt, Eastern Indian Craton

Santosh Kumar, Rama Chandrudu Arasada and Gangumalla Srinivasa Rao *

Department of Applied Geophysics, Indian Institute of Technology (Indian School of Mines), Dhanbad 826004, Jharkhand, India; santosh.19dr0183@agp.iitism.ac.in (S.K.); 22pr0036@iitism.ac.in (R.C.A.)
* Correspondence: gsrao@iitism.ac.in or vasugeos@gmail.com

Abstract: Fuzzy C-Means (FCM) clustering is an unsupervised machine learning algorithm that helps to integrate multiple geophysical datasets and provides automated objective-oriented information. This study analyzed ground-based Bouguer gravity and aeromagnetic datasets using the FCM clustering algorithm to classify lithological units in the western part of the North Singhbhum Mobile Belt, a mineralized belt in the Eastern Indian Craton. The potential field signatures of clusters obtained using FCM correlate remarkably well with the existing surface geology on a broad scale. The cluster associated with the highest gravity signatures corresponds to the metabasic rocks, and the cluster with the highest magnetic response represents the mica schist rocks. The cluster characterized by the lowest gravity and magnetic responses reflects the granite gneiss rocks. However, few geological formations are represented by two or more clusters, probably due to the close association of similar rock types. The fuzzy membership scores for most of the data points in each cluster show above 0.8, indicating a consistent relationship between geophysical signatures and the existing lithological units. Further, the study reveals that integrating multi-scale geophysical data helps to disclose bedrock information and litho-units under the sediment cover.

Keywords: Fuzzy C-Means clustering; unsupervised machine learning; geological mapping; Bouguer gravity and aeromagnetic data; North Singhbhum Mobile Belt

Citation: Kumar, S.; Arasada, R.C.; Rao, G.S. Multi-Scale Potential Field Data Integration Using Fuzzy C-Means Clustering for Automated Geological Mapping of North Singhbhum Mobile Belt, Eastern Indian Craton. *Minerals* **2023**, *13*, 1014. https://doi.org/10.3390/min13081014

Academic Editors: Ahmed Mohammed Eldosouky, Stephen Eguba Ekwok and Giovanni Martinelli

Received: 22 June 2023
Revised: 26 July 2023
Accepted: 26 July 2023
Published: 29 July 2023

1. Introduction

Lithological mapping of the area has numerous imperative applications, such as targeting natural resources, estimating geological hazards, and understanding geological evolution. However, the direct lithological interpretation of the area can be challenging in the case of the soil cover regions. In such scenarios, multi-parameter ground and airborne geophysical datasets are crucial for accurately mapping the lithology. Conventionally, these geophysical datasets are processed and interpreted individually to obtain lithological information, which is time-consuming, and the success of interpretations is highly dependent on the user's experience. Data-driven approaches have proven to be effective for automatically extracting information from one or multiple co-located datasets [1–5]. Before machine learning (ML), weights of evidence (WofE) was widely used for automatic lithological mapping and mineral prospectivity modeling (MPM) [6–10]. One main drawback of WofE is that the analysis requires an independent thematic map, and the target layer must include the known points of interest [11]. As a result, it may not be appropriate for small areas containing the targets of interest. Another limitation of this method is the uncertainty in interpreting the target depth when constructing a 3D geological model based on the geological cross sections [8].

Recently, supervised and unsupervised ML algorithms have emerged to interpret geoscience datasets due to their remarkable capability in identifying the nonlinear relationships between known lithologies and geophysical anomalies [1,3–5,12–17]. Both methods have their own advantages and disadvantages. Building an appropriate supervised ML model requires training the model with sufficient known label datasets, which can be tedious, especially when dealing with big datasets. On the other hand, unsupervised ML algorithms such as crisp or fuzzy cluster analysis do not require such labeled datasets, and they provide different clusters based on the similarities or patterns of the datasets [18,19]. A crisp clustering algorithm, for example, k-means clustering analysis, assigns each data point to its nearest cluster center without ambiguity [18]. In contrast, fuzzy clustering analysis allows each data point to have some degree of fuzzy membership regarding the other clusters [19]. This fuzzy membership degree indicates the quantitative significance of a data point belonging to a particular cluster.

Several researchers have successfully used crisp clustering algorithms for lithological differentiation and exploration targets using remote sensing and ground-based geophysical datasets [3,20–25]. In recent years, fuzzy clustering analysis has gained popularity as it allows for quantitative assessment of the identified clusters [1,3,5,26]. Similar to crisp clustering, fuzzy clustering analysis has been used to integrate multiple geophysical datasets for automated geological/geochemical mapping and mineral exploration [1,3,5,26], as well as petrophysical characterization [4,27–29]. One of the drawbacks of applying pixel-based cluster analysis methods is that they may pose challenges due to the lack of distinct clustering in the overall dataset. Similar issues arise when processing thin-section images using cluster analysis and seismic datasets [8,30]. To mitigate these drawbacks, a possible solution is to employ the characteristic analysis developed by Botbol et al. for geochemical prospection [31–33]. Essentially, this method involves working within a neighborhood window or template around a pixel location rather than solely focusing on the pixel itself. Another approach is the factorial kriging analysis, which takes into account the spatial structures [34,35].

The present study utilizes the Fuzzy C-Means (FCM) clustering algorithm with the aim of integrating ground gravity and airborne magnetic datasets for automated geological mapping of the western part of the North Singhbhum Mobile Belt (NSMB). Initially, we performed feature engineered procedures on ground gravity and airborne magnetic datasets to provide unbiased input to the FCM clustering algorithm. Subsequently, we generated a geo-attributed cluster map (pseudo lithological map) of the NSMB based on the correlation between the integrated geophysical signatures of FCM clusters and the existing surface geological map. Furthermore, the study also computes the fuzzy membership score of each cluster to quantitatively assess the relationship between the geophysical signatures of the cluster and litho-units.

2. Study Area

The study area covers a latitude range from 22.75° to 23.25° N and a longitude range from 85.75° to 86.00° E within the NSMB and the southernmost part of the Chotanagpur Granite Gneiss Complex (CGGC) (Figure 1). The area is of great importance for understanding the geodynamic and metallogenic evolution of the Eastern Indian Shield [36–40]. Within the study area, five distinct geological domains are identified, namely CGGC, Chandil, Dalma, Dhalbhum, and Chaibasa Formations (Figure 1). The CGGC portion primarily consists of granite gneiss rocks with minor porphyritic granitoid [41,42]. The remaining four formations belong to the NSMB and are separated from the CGGC by the South Purulia Shear Zone (SPSZ). The Chandil Formation comprises phyllite, quartz-mica schist with interbedded phyllite (QMSIP), carbon phyllite, metabasic, and acid-tuff rocks [43–46]. The Dalma Formation is characterized by metabasic and ultrabasic rocks with carbonate lenses [43–46]. The Chaibasa and Dhalbhum Formations consist of phyllite, mica schist, rhyolite, and chlorite phyllite/sericite muscovite schist (CP/SMS) rocks [45,46].

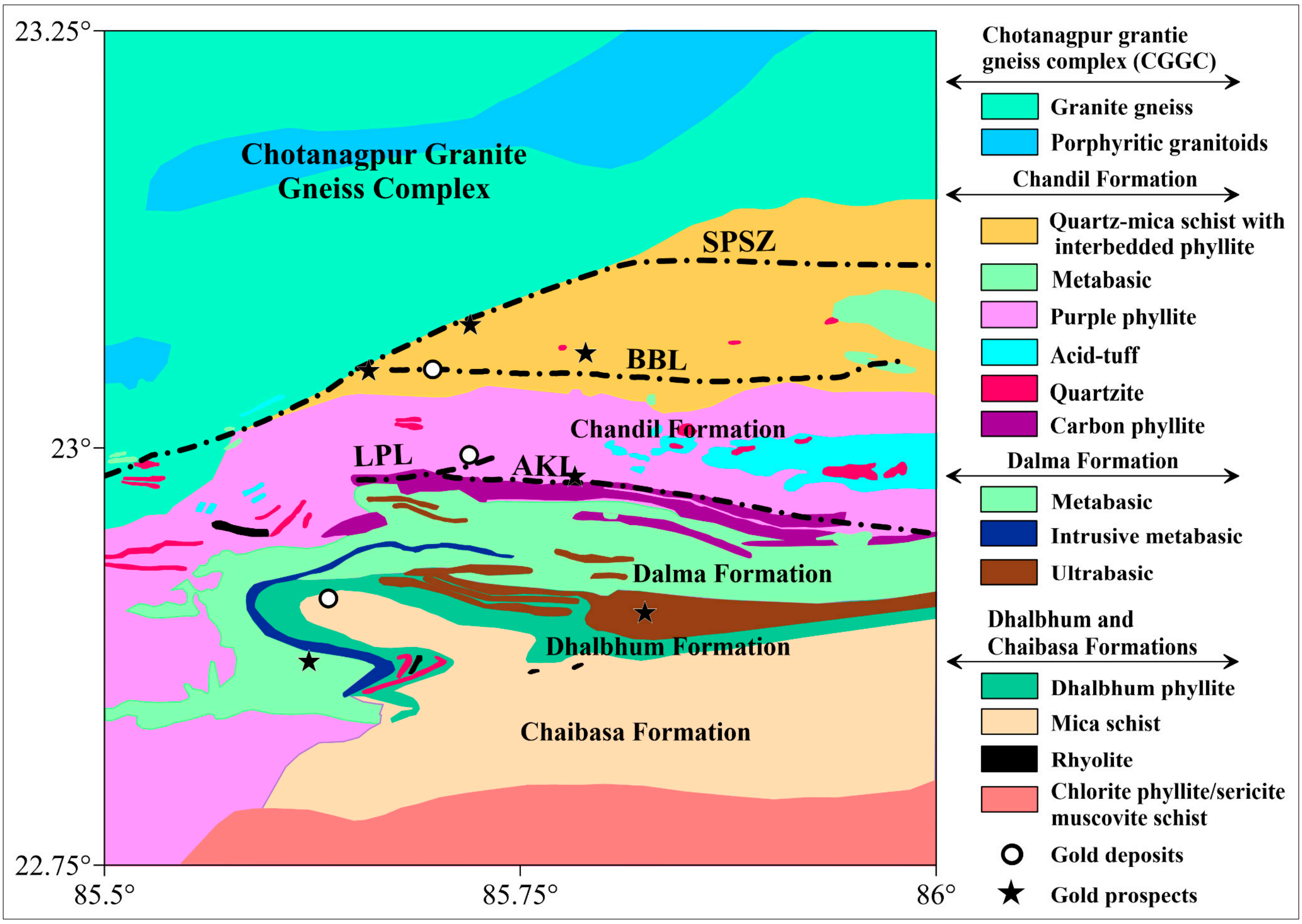

Figure 1. Illustration of the detained geological map of the western North Singhbhum Mobile Belt (NSMB) (modified after Chaudhuri and Roy [36]). Black dashed-dotted lines represent the lineaments/shear zones. AKL: Antabera–Kuda lineament; BBL: Babaikundi–Birgaon lineament; LPL: Lungtu–Parasi lineament; SPSZ: South Purulia Shear Zone.

Based on geochemical and petrographical studies, previous researchers have reported gold deposits and potential gold zones within the Chandil and Dalma Formations [36,39,47–51] (Figure 1). In the Chandil Formation, gold mineralization occurs within the quartz reef rocks near the Babaikundi–Birgaon lineament, where mica schist serves as the host rock [36,47]. In the Dalma Formation, gold mineralization is found along the sheared contact of volcanic tuffs, sheared quartzites, and phyllite rocks along the Lungtu–Parasi lineament [39,52–54]. Along the Antabera–Kudda lineament, gold mineralization is observed in the ferruginous quartzites and quartz veins interacting with phyllites and metabasic rocks [50].

3. Data and Methodology

In order to characterize the geology of the study area, we utilized ground gravity and airborne magnetic datasets. The workflow of the FCM clustering algorithm implemented in this study is illustrated in Figure 2. The ground gravity data consisted of approximately 1085 observations taken along all available roads, with a spacing of approximately 1.5–2.0 km. These observations were acquired using the Scintrex CG-5 Autograv gravimeter, which has a precision of 0.001 mGal. The airborne magnetic datasets were collected between 1968 and 1969 by the Geological Survey of India as part of the Operation Hard Rock (OHR) program [55]. The survey involved north–south oriented lines spaced 0.5 km apart and was conducted at terrain-corrected heights of 61 m and 122 m. The gravity observations were subjected to standard corrections, including latitude, free-air, Bouguer, and terrain corrections, to derive the Bouguer gravity anomaly.

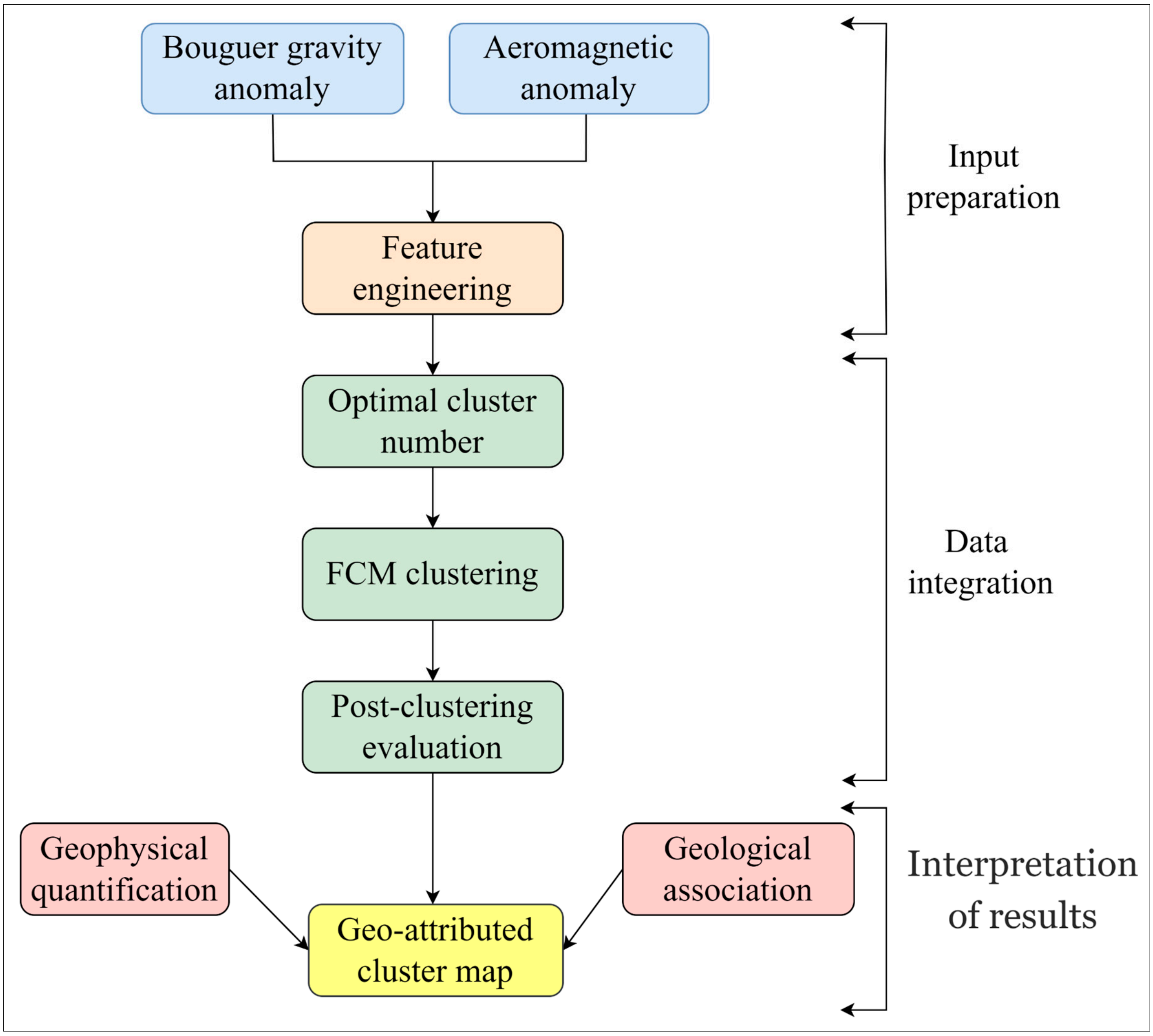

Figure 2. Flowchart illustrating the integration of the Bouguer gravity and aeromagnetic anomalies using the Fuzzy C-Means clustering algorithm.

Similarly, the magnetic observations were corrected for the Earth's main magnetic field using a suitable International Geomagnetic Reference Field (IGRF) model to obtain the magnetic anomaly. Additionally, the regional-residual separation of Bouguer gravity and magnetic anomalies was carried out as they contain information from anomalous sources with different depths and different densities or magnetizations. For this purpose, upward continuation filtering was applied to the Bouguer gravity and magnetic anomalies to obtain the long wavelength signatures associated with deep-seated sources [56]. These long wavelength signatures were further subtracted from Bouguer gravity and magnetic anomalies to obtain the residual Bouguer gravity/magnetic anomalies. To utilize these datasets in our study, we generated residual Bouguer gravity (Figure 3a) and magnetic anomaly maps (Figure 3b) using a uniform grid spacing of 500 m, resulting in 10,201 samples. The corresponding data distributions are presented in Figure 3c,d, respectively.

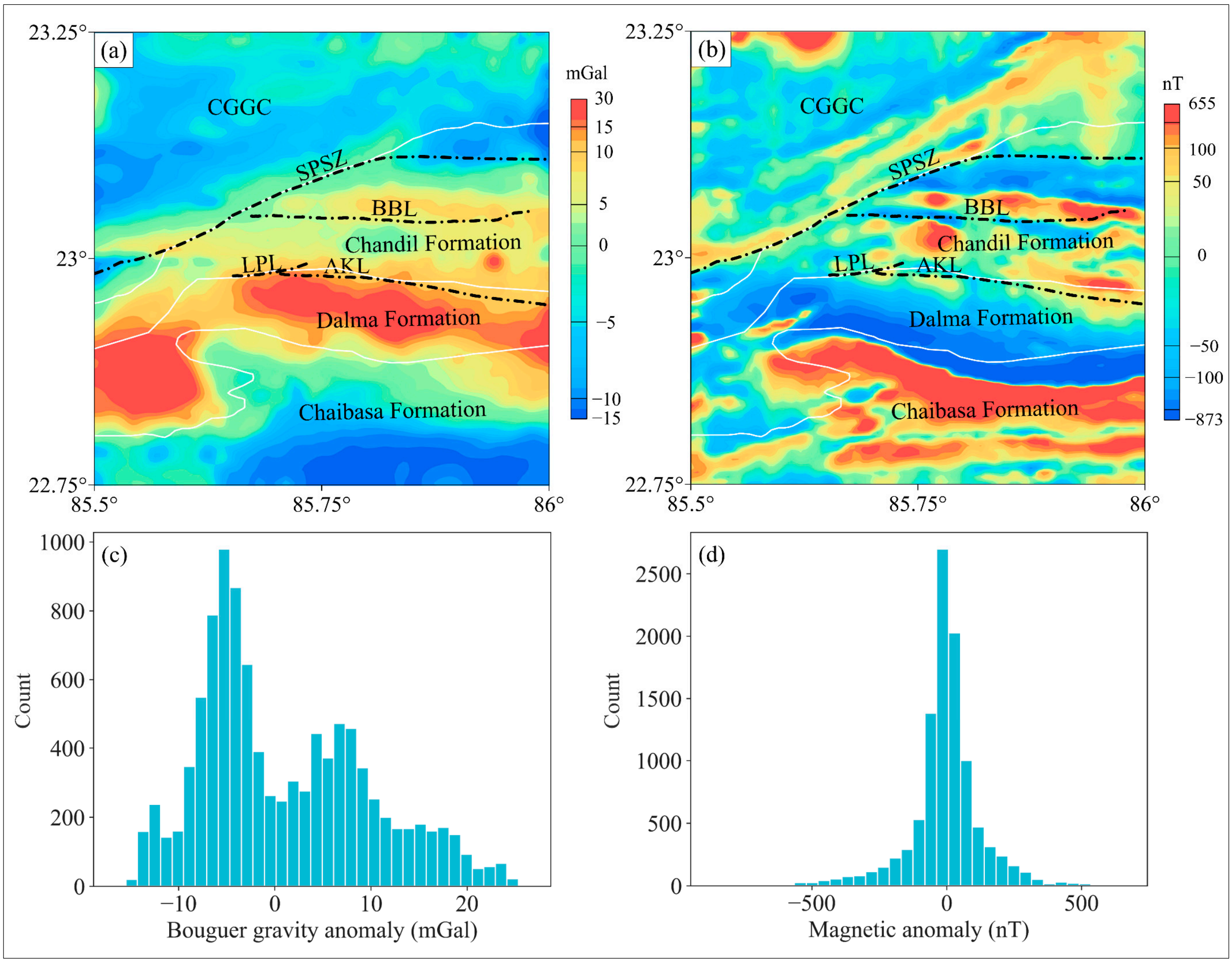

Figure 3. (**a**) Bouguer gravity and (**b**) magnetic anomalies maps were generated with a regular grid interval spacing of 500 m. Corresponding histogram plots are shown in (**c**) and (**d**), respectively. In Figure 3a,b, black dashed-dotted lines represent lineaments/shear zones, while solid white lines indicate the major geological boundaries of the study area. AKL refers to the Antabera–Kuda lineament, BBL represents the Babaikundi–Birgaon lineament, CGGG stands for Chotanagpur Granite Gneiss Complex, LPL denotes the Lungtu–Parasi lineament, and SPSZ represents the South Purulia Shear Zone.

3.1. Fuzzy C-Means (FCM) Clustering Algorithm

The Fuzzy C-Means (FCM) clustering algorithm [19] is an unsupervised ML method used to discover patterns or structures in data and group similar data points together. The primary objective of this method is to maximize the similarity among data points within clusters and minimize the similarity between clusters. In this approach, each data point is assigned to real values between '0' and '1', known as membership degrees [19]. The sum of membership degrees for data points across all clusters is equal to '1'. The magnitude of membership degrees indicates the degree of belongingness to each cluster. To identify the optimal fuzzy c-partitions, the least square error function is defined using the following equation [19]:

$$J_{FCM}(U, V) = \sum_{i=1}^{c}\sum_{k=1}^{n}(u_{ik})^{m}\| x_k - v_i \|^2 \quad \text{dependent upon } \sum_{i=1}^{c} u_{ik} = 1, \tag{1}$$

where n is the total number of data points $(x_1, x_2, x_3, \cdots, x_k, \cdots x_n)$; c is the total number of clusters; m is the weighting exponent $(1 \le m < \infty)$, which controls the degree of fuzziness; and $V = \{v_1, v_2, v_3 \cdots v_c\}$ specifies the location of center points. $U = \{u_{ik} \in [0, 1]\}$ is the membership matrix where each element (u_{ik}) represents the membership degree of i-th data point to the k-th cluster. The symbol $\| \, . \, \|$ denotes the Euclidean norm, which measures the degree of similarity between the data point and the center point. The center point (v_i) of the ith cluster is determined using the following equation [19]:

$$v_i = \frac{\sum_{k=1}^{n}(u_{ik})^m x_k}{\sum_{k=1}^{n}(u_{ik})^m} \tag{2}$$

Further, each element (u_{ik}) of the U matrix can be calculated using the following equation [19]:

$$u_{ik} = \left[\sum_{a=1}^{c}\left(\frac{d_{ik}}{d_{ak}}\right)^{2/(m-1)}\right]^{-1} \quad \text{subjected to } d_{ik}^2 = \| \, x_k - v_i \, \|^2 \tag{3}$$

To determine the optimal values of centers and membership degrees, the algorithm iteratively calculates the U and V matrixes for each data point. This process begins by providing initial parameters, including the number of clusters, the weighting exponent m, and an initial estimation of either the membership matrix U or the matrix V representing the cluster center locations. The matrix V is determined from the membership matrix U using Equation (2), while the membership matrix U is determined from the matrix V using Equation (3). This iterative process continues until the norm of the updated membership matrixes U^k and U^{k+1} for two consecutive steps (k-step and k + 1 step) falls below a predetermined threshold value ε. At this point, the algorithm converges and provides the final membership degrees and cluster center locations.

3.2. Feature Engineering

In order to achieve optimal performance of ML algorithms, it is important to have appropriate input features. This process, known as feature engineering [57], involves transforming raw datasets into suitable input features for ML algorithms. Essentially, before applying ML algorithms, it is necessary to pre-process the raw datasets using feature engineering techniques such as imputation, binning, outlier handling, filtering, log transformation, scaling, etc. This ensures better algorithm performance. In this study, we utilized the Fuzzy C-Means (FCM) clustering algorithm, an unsupervised ML algorithm, to analyze the Bouguer gravity and aeromagnetic datasets. The FCM clustering algorithm operates based on Euclidian distance [19,58], and the resulting clusters tend to exhibit a spherical shape. However, input datasets with long-tailed or skewed distributions can pose challenges in achieving optimal clustering results. Therefore, it is crucial for all input features to exhibit relatively normal distributions within the data domain, without significant long tails and skewed distributions.

The Bouguer gravity and magnetic anomaly data are illustrated in Figure 3a,b, respectively. Their corresponding histogram plots are shown in Figure 3c,d, respectively. The data distribution of the Bouguer anomaly exhibits a bimodal nature, indicating the presence of two distinct modes or peaks (Figure 3c). On the other hand, the magnetic anomaly distribution displays long tails, indicating the occurrence of extreme values (Figure 3d). Based on the observed data distributions, we employed various feature engineering techniques to enhance the specific datasets. For the Bouguer gravity, we utilized its vertical gradient anomaly data to magnify the signatures of shallow subsurface source bodies. To eliminate dipolar signatures in the magnetic data, we applied a step-by-step feature engineering process. Step 1 involved computing the vertical gradient of the magnetic data to enhance the shallow body signatures (Figure 4a) [59,60]. The corresponding histogram plot is presented in Figure 4d, showing a more condensed distribution around zero (Figure 4d). Step 2 entailed taking the absolute values of the vertical gradient magnetic data to eliminate negative values (Figure 4b). The corresponding data distribution is displayed in Figure 4e, revealing a highly skewed shape with a long tail. To address this skewness and long tail, step 3 involved applying a logarithmic transformation to the absolute vertical gradient magnetic data. This transformation resulted in consistent magnetic signatures (Figure 4c,f). After performing these steps, we applied a low-pass filter technique to both datasets to attain suitable data distribution and ensure their compatibility. Finally, we applied the normalization technique to both datasets to obtain comparable datasets in the clustering parameter space. The feature engineered gravity and magnetic datasets are displayed in Figure 5a,b, respectively, whereas their data distribution is shown in Figure 5c,d, respectively. Figure 6 demonstrates the data distribution in the 2D cross-plots of the Bouguer gravity and magnetic anomalies before and after the feature engineering.

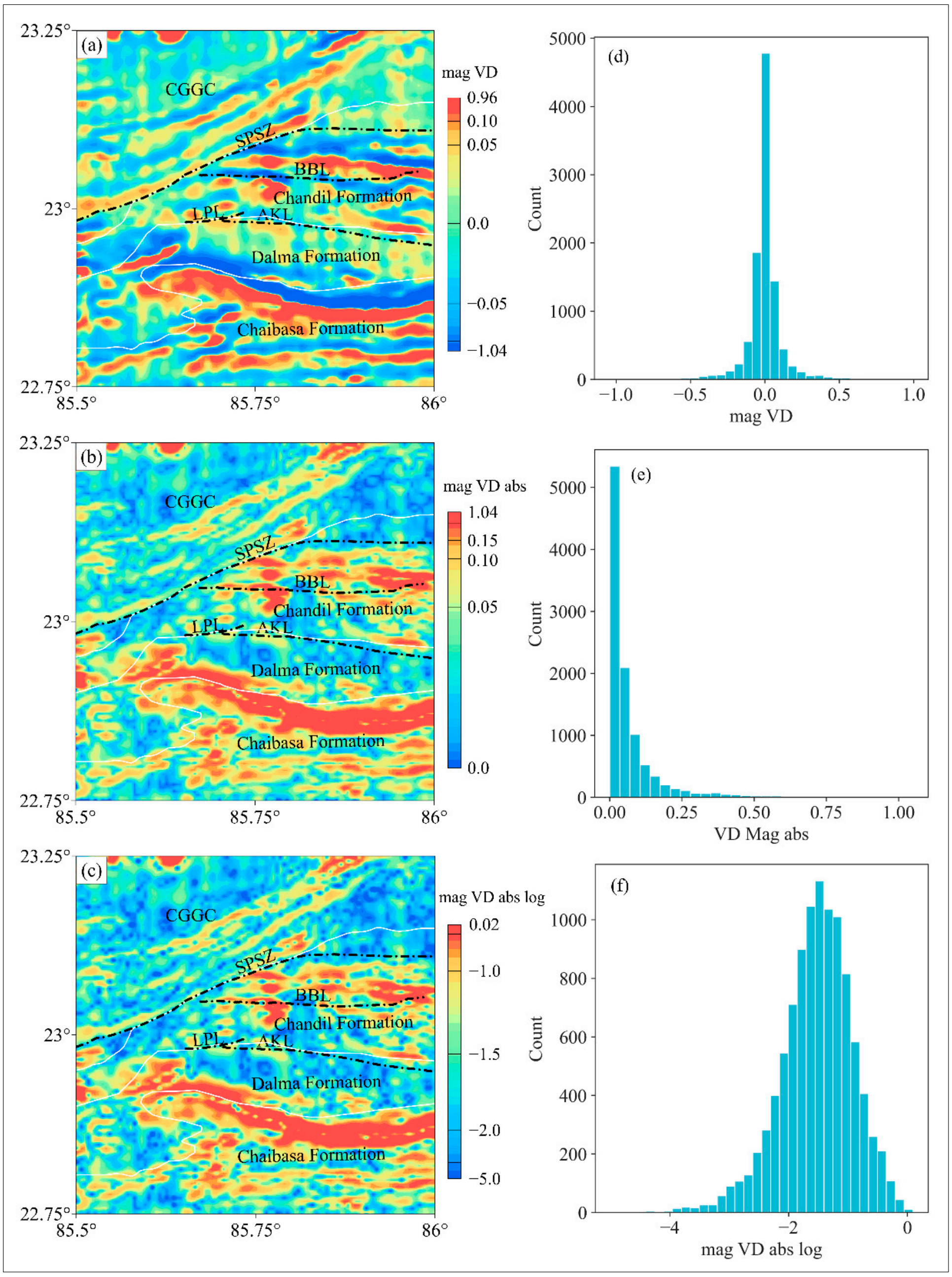

Figure 4. Stepwise feature engineering procedure for the magnetic anomaly data. (**a**) Vertical derivative of the magnetic anomaly. (**b**) Absolute values of the vertical derivative of the magnetic anomaly. (**c**) Logarithm transformation ($\log_{10}$) of the absolute vertical derivative of the magnetic anomaly. Plots (**d**–**f**) illustrate the corresponding feature engineered magnetic anomaly data distributions for (**a**–**c**), respectively. The other details displayed on the maps (Figure 4a–c) are identical to Figure 3.

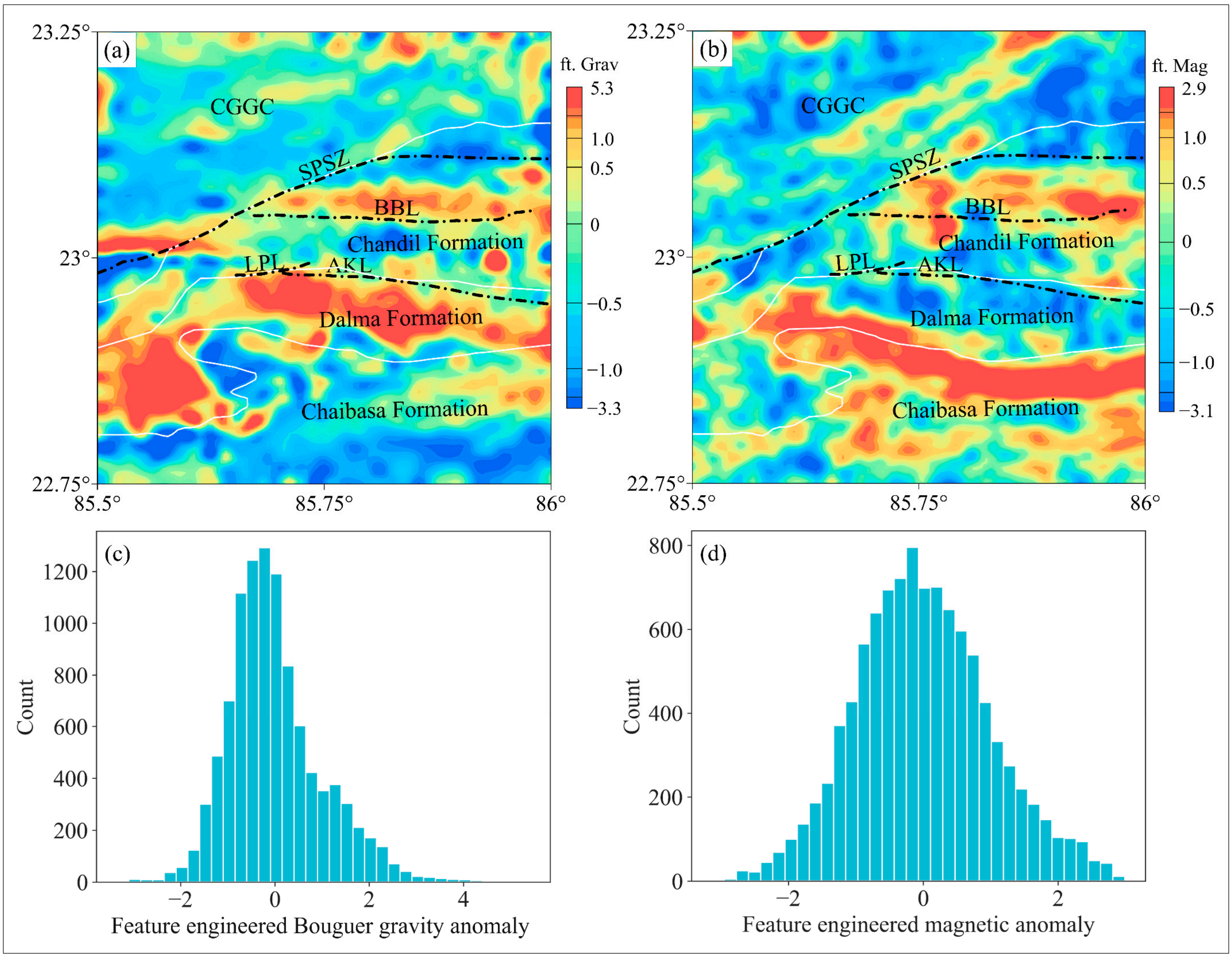

Figure 5. The feature engineered (**a**) Bouguer gravity and (**b**) magnetic anomaly maps are depicted, along with their corresponding data distribution plots (**c**) and (**d**), respectively. The other details shown in Figure 5a,b are identical to those presented in Figure 3.

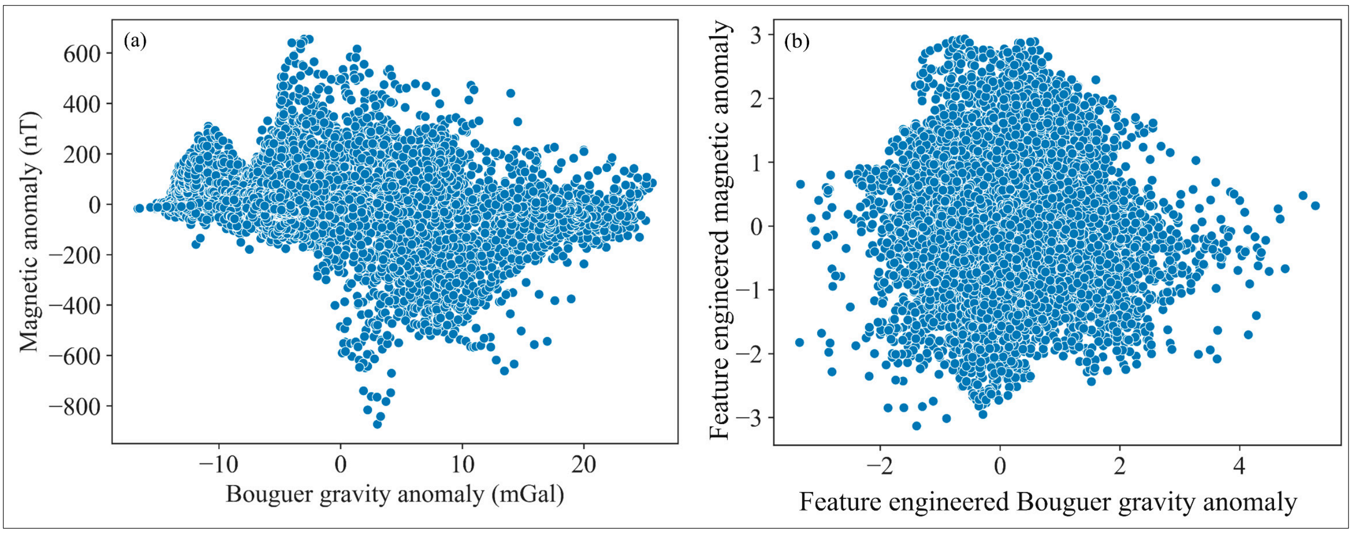

Figure 6. The 2D cross-plots of the Bouguer gravity and magnetic anomalies are shown before (**a**) and after (**b**) feature engineering.

3.3. Optimal Cluster Number Selection

In order to utilize the FCM clustering algorithm effectively, determining the appropriate number of clusters for a given dataset is necessary. In the present study, the optimal clustering number was determined by comparing the results obtained from three distinct mathematical techniques: the Elbow method [61], the Caliński–Harabasz score [62], and the Silhouette score [63]. The Elbow method calculates the Within-Cluster Sum of Squares (WCSS), which is the sum of the squared distances between each point and the centroid within a cluster. The WCSS values are plotted on a graph against the number of clusters. The optimal number of clusters is identified at the point where the steep slope of the curve changes to a gentle slope, forming a characteristic 'elbow shape'. The Caliński–Harabasz score, also known as the variance ratio criterion, assesses the dispersion of data points within their respective cluster and their separation from other clusters. It is calculated as the ratio between the sum of intracluster variance and the sum of the intercluster variance. A higher Caliński–Harabasz score indicates well-defined clusters within the data. The Silhouette index measures the closeness of each data point to its own cluster compared to the other clusters. It ranges from −1 to +1, where scores closer to +1 indicate well-defined clusters within the dataset, and scores close to −1 indicate incorrect clustering. By considering the results from these three techniques, the optimal number of clusters can be determined, ensuring the best representation of the underlying patterns in the data.

In this study, all three methods were computed across a cluster range of 2 to 14 to determine the optimal cluster number. Figure 7a–c present the WCSS values obtained from the Elbow method, the Caliński–Harabasz score, and the Silhouette score, respectively. The graph plot of the Elbow method reveals a distinct Elbow pattern at cluster number 4, indicating a potential optimal cluster number (Figure 7a). The Caliński–Harabasz score shows the highest score at cluster number 4, followed by cluster numbers 3 and 5, suggesting these as potential optimal cluster numbers (Figure 7b). In the Silhouette score analysis, the highest score is observed at cluster number 3, followed by the second-highest score at cluster number 4 (Figure 7c). Considering the results from the three mathematical criteria, both the Elbow method and Caliński–Harabasz score suggest cluster number 4 as the optimal choice. In the Caliński–Harabasz score analysis, cluster numbers 3 and 5 appear to be optimal choices. It is worth mentioning that determining the optimal cluster number can depend on the specific method employed and the user's experience, as suggested by Wang et al. [5]. Although cluster number 4 was deemed optimal based on the three mathematical criteria discussed earlier, it may not fully capture the complexity of the study area's geology. Therefore, it is important to acknowledge that capturing the intricate geology of the study area requires a more nuanced and comprehensive approach. Therefore, cluster number 5 was selected as the best compromise between mathematical criteria and the need to accurately represent the geological information through FCM clustering analysis.

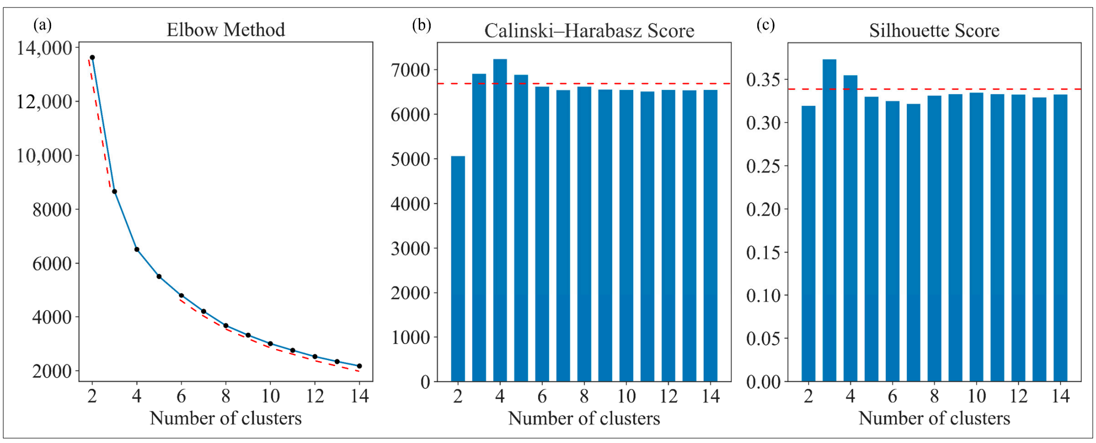

Figure 7. Cluster performance evaluation is based on three different mathematical approaches (**a**) the Elbow method, (**b**) the Calinski–Harabasz score, and (**c**) the Silhouette score for selecting the optimal

cluster number for Bouguer gravity and aeromagnetic datasets. In panel (**a**), the dashed red lines specify the steeper and gentler slopes on either side of the elbow, helping to identify the optimal cluster number. In panel (**b**), the dashed red lines mark the higher performance scores of cluster numbers 3–5, contrasting with the lower performance scores of cluster numbers 2 and 6–14. In panel (**c**), the dashed red lines separate the higher performance scores of cluster numbers 3 and 4 from the lower performance scores of cluster numbers 2 and 5–14, providing insights into the optimal cluster number.

4. Results and Interpretation

The feature engineered gravity and magnetic anomalies exhibit a normal distribution with amplitudes ranging from −3.3 to 5.3 ft. for gravity and −3.1 to 2.9 ft. for magnetic anomalies (Figure 5). The clusters obtained from the FCM clustering algorithm are displayed in the 2D cross-plot of the feature-engineered gravity and magnetic anomalies (Figure 8). Additionally, to understand the characteristics of clusters, the mean, standard deviation, and minimum/maximum values were calculated for each cluster. The results of the statistical analysis are illustrated in Figure 9, with the horizontal axis representing the cluster number and the vertical axis indicating the value range for each feature. It is important to note that the relative characteristics (high/low) of the feature engineered values are more significant in differentiating the geology rather than their absolute amplitudes. Therefore, higher feature engineered values in a cluster indicate higher gravity and magnetic anomaly values, while lower feature engineered values indicate lower gravity and magnetic anomaly values.

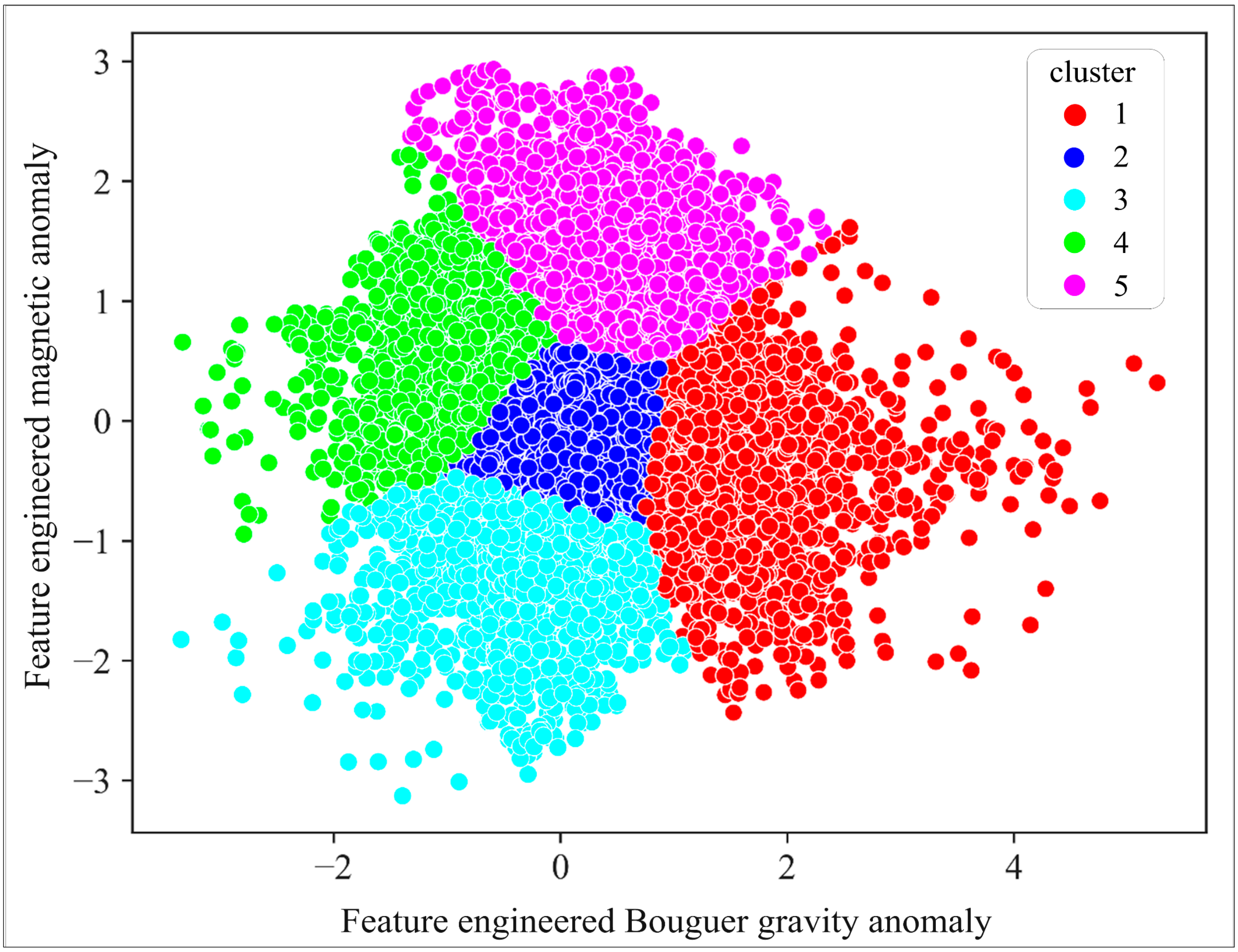

Figure 8. The 2D cross-plot illustrates the clusters of the feature-engineered Bouguer gravity and magnetic anomalies obtained from the Fuzzy C-Means clustering algorithm.

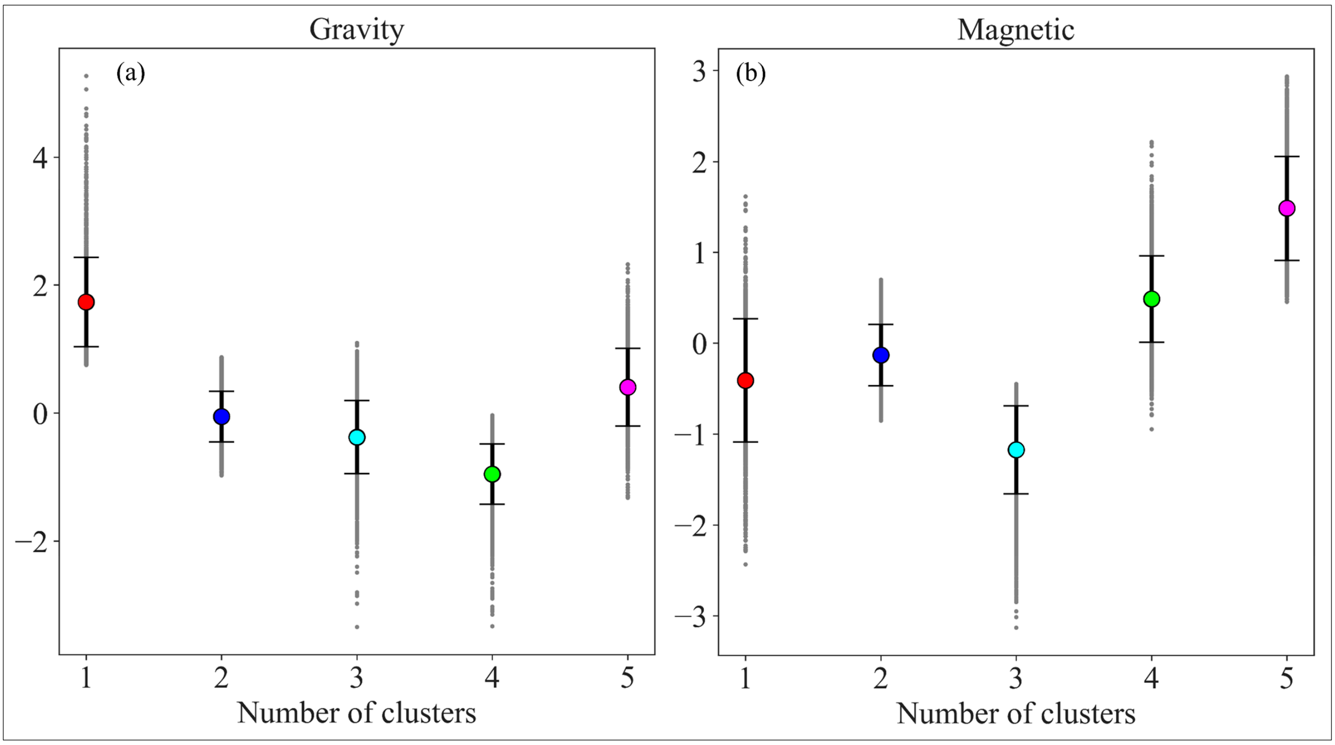

Figure 9. Illustrates the results of statistical analysis for each cluster in both feature domains, namely the (**a**) Bouguer gravity and (**b**) magnetic anomalies. The x-axes in both plots represent the number of clusters, ranging from 1 to 5, while the y-axes represent the amplitude range of feature engineered values. The y-axis amplitude range displayed in these plots corresponds to the Bouguer gravity and magnetic feature engineered values presented in Figure 5a,b, respectively. Each cluster is represented by a solid circle of different colors, indicating the mean value of that cluster. The solid black line interval on both sides of the mean denotes the standard deviation of cluster values. The dotted gray lines represent the minimum and maximum values of the clusters.

Table 1 displays the gravity and magnetic attributes of each cluster based on the statistical comparison (Figure 9). It is evident that all clusters exhibit distinct gravity and magnetic anomaly characteristics. Cluster 1 demonstrates the highest gravity and intermediate magnetic characteristics (Figure 9 and Table 1). Conversely, cluster 5 exhibits the highest magnetic attributes and intermediate gravity anomaly characteristics (Figure 9 and Table 1). Cluster 4 displays the lowest gravity and higher magnetic responses, while cluster 3 is characterized by the lowest magnetic attributes and intermediate gravity anomalies. Cluster 2 represents intermediate gravity and magnetic attributes. Additionally, it is worth noting that the signature of cluster 2 overlaps with the gravity attributes of cluster 3 and the magnetic attributes of cluster 1 (Figure 9 and Table 1).

In order to assign the geological attributes to the five cluster zones obtained from FCM clustering analysis, we overlaid the pre-existing surface geology details (Figure 1) onto the cluster map (Figure 10). Cluster 1 appears at two distinct locations on the cluster map (Figure 10). The first location is at the center of the cluster map, displaying an east-west trend and exhibiting a strong correlation with the metabasic rocks of the Dalma Formation (Figure 10 and Table 1). The second location is nearly circular and lies in the southwestern portion of the cluster map. It shows a strong correlation with both the metabasic rocks of the Dalma Formation and the phyllite rocks of the Chandil Formation.

Table 1. Summary of the FCM clustering analysis based on ground Bouguer gravity and airborne magnetic datasets and the corresponding geological attributes.

Cluster	Gravity Attributes	Magnetic Attributes	Geological Association
Cluster 1	Highest	Intermediate	Metabasic and phyllite rocks
Cluster 2	Intermediate	Intermediate	Granite gneiss, phyllite, acid-tuff, quartz-mica schist with interbedded phyllite (QMSIP), and mica schist rocks
Cluster 3	Intermediate	Lowest	Granite gneiss, phyllite, and QMSIP rocks
Cluster 4	Lowest	Higher	Chlorite phyllite/sericite muscovite schist (CP/SMS), granite gneiss, and mica schist rocks
Cluster 5	Intermediate	Highest	Phyllite, mica schist, and QMSIP rocks

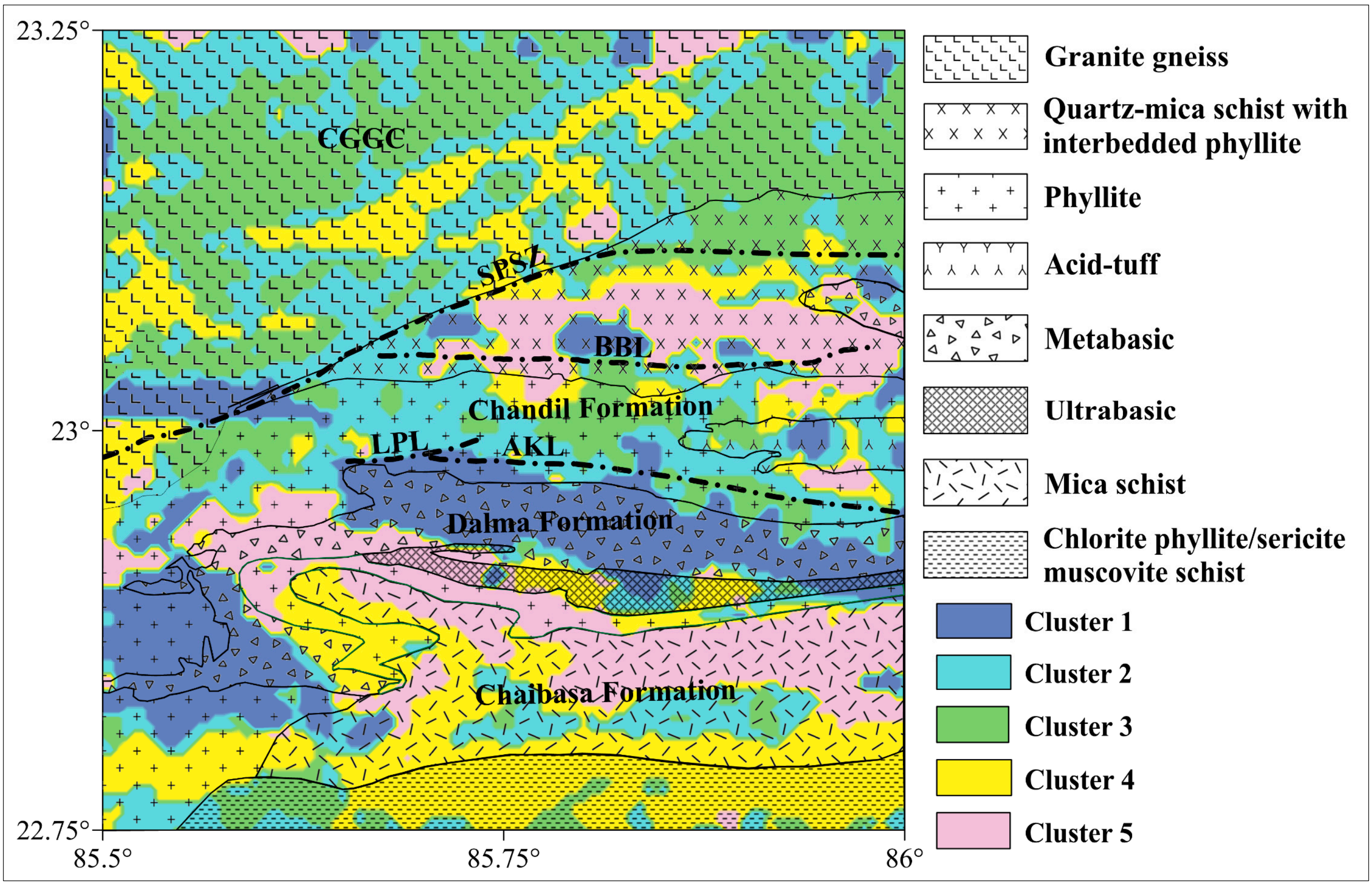

Figure 10. The cluster map obtained from the FCM clustering algorithm overlaid with a simplified geological map of the study area. The other information shown on the map is the same as in Figure 3.

Among all five clusters, cluster 2, which is characterized by intermediate gravity and magnetic signatures (Table 1), does not correspond to any unique geological formation and spreads irregularly across the study area as patches (Figure 10). In the northern part, occurrences of cluster 2 are found over the granite gneiss rocks of the CGGC, phyllite, and acid-tuff rocks of the Chandil Formation. In the southern part, occurrences of cluster 2 are found over the mica schist rocks of the Chaibasa Formation and QMSIP rocks of the Chandil Formation.

Cluster 3 occurrences are predominantly associated with granite gneiss rocks of the CGGC region (Figure 10 and Table 1). However, a few occurrences of cluster 3 appear over the central and northern portions of the Chandil Formation, which are associated with the phyllite and QMSIP rocks. It is also observed that cluster 2 is surrounded by cluster 3 in most areas due to minor differences in their gravity characteristics, indicating that both clusters might represent similar rock types but may be under soil cover/associated with different rock types (Figure 10 and Table 1). On the other hand, cluster 4 occurrences primarily cover the southernmost portion of the Chaibasa Formation. The major rock types in this region are mica schist and CP/SMS rocks, which align with the low gravity and intermediate magnetic responses displayed by cluster 4. Additionally, the central portion of the CGGC also appears as a prominent area for cluster 4, and it is associated with granite gneiss rocks with a northeast–southwest trend. Similar to cluster 1, cluster 5 also displays an east–west trend and shows predominant occurrences over the Chandil Formation and Chaibasa Formation. More specifically, the mica schist rocks of the Chaibasa Formation and QMSIP rocks of the Chandil Formation are represented by cluster 5, which exhibits intermediate gravity and the highest magnetic characteristics (Figure 10 and Table 1).

Table 2 presents the conditional probabilities of the specific rock-type units within each cluster, with rows representing the cluster number and columns specifying the various rock types. In cluster 1, metabasic rocks display the highest probability of 0.66. Following this, ultrabasic and phyllite rocks show higher probabilities of 0.23 and 0.22, respectively. In cluster 2, acid-tuff, granite gneiss, and phyllite rocks are associated with relatively equal probabilities of 0.42, 0.31, and 0.29, respectively. Similar probabilities are found for the phyllite (0.42) and QMSIP (0.23) rocks in cluster 3. Cluster 4 exhibits the highest probability of 0.7, corresponding to the CP/SMS, and following this, mica schist, ultrabasic, and acid-tuff rocks show relatively higher probabilities of 0.36, 0.29, and 0.21, respectively. Subsequently, cluster 5 displays the highest probability of 0.42, associated with mica schist. After this, QMSIP and ultrabasic rocks demonstrate higher probabilities of 0.35 and 0.26, respectively.

Table 2. Shows the conditional probability of the various rock types within each cluster.

		Rock Types							
		Granite Gneiss	**Quartz-Mica Schist with Interbedded Phyllite**	**Phyllite**	**Acid-Tuff**	**Metabasic**	**Ultrabasic**	**Mica Schist**	**Chlorite Phyllite/Sericite Muscovite Schist**
Clusters	C1	0.05	0.09	0.22	0.18	0.66	0.23	0.03	0
	C2	0.31	0.2	0.29	0.42	0.08	0.17	0.16	0.11
	C3	0.42	0.23	0.15	0.13	0.03	0.06	0.04	0.18
	C4	0.18	0.13	0.18	0.21	0.06	0.29	0.36	0.7
	C5	0.04	0.35	0.16	0.06	0.16	0.26	0.42	0.01

5. Discussion

On a broad scale, the five clusters obtained using FCM analysis of Bouguer gravity and aeromagnetic anomalies demonstrate a significant correlation with the major geological formations in the study area, suggesting that FCM can be a useful tool for initial geological mapping. To quantitatively relate the geophysical signatures of each cluster with pre-existing surface geology, the fuzzy membership scores were determined for each data point in every cluster (Figure 11). A fuzzy membership score higher than 0.8 was considered a reliable indicator for assigning the geological attributes to the cluster responses of geophysical data. For cluster 1, fuzzy membership scores > 0.8 were found for the metabasic rocks of the Dalma Formation (Figure 11a). It is worth noting that the trustworthiness responses (fuzzy score > 0.8) of cluster 2 appear to be scattered in nature, indicating a less clear association with a specific geological formation (Figure 11b). The high fuzzy membership scores (>0.8) of clusters 3 and 4 correspond to the granite gneiss rocks of the CGGC (Figure 11c,d). Additionally, the high fuzzy membership scores (>0.8) of cluster 4 are linked to the mica schist and CP/SMS rocks of the Chaibasa Formation (Figure 11d). The mica-schist rocks of the Chaibasa Formation and QMSIP rocks of the Chandil Formation exhibit a trustworthiness value (>0.8 fuzzy scores) in cluster 5 (Figure 11e).

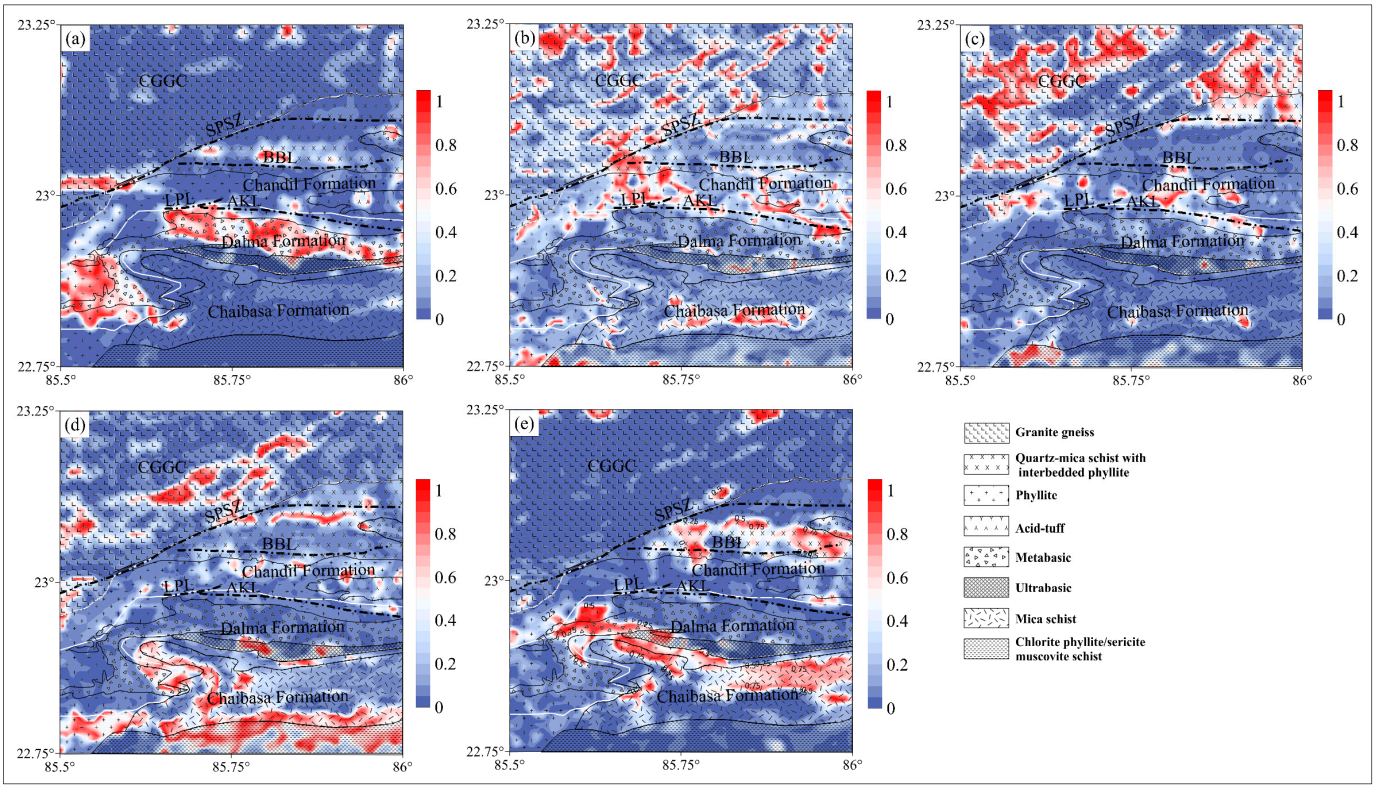

Figure 11. (**a**–**e**) Demonstrate the fuzzy membership scores of each cluster (1–5) generated by the FCM clustering algorithm. The remaining details displayed on all maps are the same as in Figure 3.

Nevertheless, the clustered zone map captures all the major geological formations with high fuzzy scores (>0.8) on a broad scale. However, some inconsistencies are observed when comparing the existing surface geology map at a more detailed level. Previous studies [1,5,26] have also highlighted similar discrepancies between clustering results and bedrock geology at a more refined scale. These inconsistencies are attributed to the limitation of having a limited number of clusters, which may not be sufficient to accurately map the geology of larger areas or more complex regions [1,5,26]. It is important to note that the five-cluster zone map presented in this study represents the objective integration of gravity and magnetic datasets, which have different penetration depths. Magnetic anomalies capture source bodies up to Curie depth, while gravity anomalies reflect anomalous density contrasts from all depths down to the surface. Therefore, the integrated cluster map contains multi-depth information, making it challenging to establish a direct correlation between the clustering results and pre-existing surface geology of the study area.

Statistical analysis conducted in this study also indicates that few clusters exhibit overlapping signatures in specific features, suggesting that these clusters consist of similar rock types. For example, clusters 2 and 3 display identical gravity attributes but differ in magnetic characteristics (Figure 9). Similarly, clusters 1 and 2 demonstrate intermediate magnetic anomaly characteristics, indicating minimal variation in rock types between these clusters. However, they differ significantly in gravity, with cluster 1 having a higher mean vertical gravity gradient than cluster 2. This difference in gravity assists in mapping rock types beneath the sediment cover (Figure 9). Additionally, all five clusters represent the ultrabasic rocks of the Dalma Formation and the acid-tuff rocks of the Chandil Formation, suggesting the possibility of merging these regions with other rock types (Figure 10). These findings suggest that relying solely on gravity and magnetic anomalies in clustering analysis may not be sufficient to capture all the rock types present in the study area. It is worth mentioning that airborne magnetic and gravity responses are often associated with variations in mineral content, such as the presence of minerals like pyrrhotite or magnetite. The absence of elemental or mineralogical data makes it challenging to identify rock facies based solely on gravity and magnetic responses. Integrating geochemical and additional geophysical datasets relevant to the study, along with gravity and magnetic anomalies, can increase the number of clusters and provide more detailed information on the geology map. Furthermore, incorporating petrophysical information in the analysis would contribute to validating the geological attributes inferred from the FCM clustering algorithm using geophysical datasets.

6. Conclusions

This study utilized the FCM clustering algorithm to differentiate the various lithological units in the western part of the NSMB region using ground-based Bouguer gravity and aeromagnetic datasets. The key findings of this study can be summarized as follows:

- The FCM clustering analysis identified five clusters with distinct geophysical signatures, each corresponding to a specific rock type. Clusters associated with the highest gravity responses are found in the metabasic rocks of the Dalma Formations, while clusters with the highest magnetic signatures were associated with the mica schist rocks of the Chaibasa Formations. Clusters displaying the lowest gravity and magnetic characteristics were observed over the granite gneiss rocks of the Chotanagpur granite gneiss complex.
- The fuzzy membership scores of most data points in each cluster exceed 0.8, indicating a strong relationship between the geophysical attributes and existing lithological units.
- On a broad scale, the results of FCM clustering analysis demonstrated a strong spatial correlation with the existing geological map. However, at a more detailed geological scale, some inconsistencies were observed between the cluster responses and known surface geological units. These inconsistencies could be attributed to the limited number of clusters used in the FCM analysis. Therefore, integrating other relevant geophysical information with the gravity and magnetic datasets can help increase the number of clusters and address these inconsistencies. Overall, the FCM clustering analysis provided valuable insights into the lithological differentiation in the study area and demonstrated the potential of integrating geophysical data for geological mapping.

Author Contributions: Conceptualization, S.K., R.C.A. and G.S.R.; methodology, S.K., R.C.A. and G.S.R.; software, S.K., R.C.A. and G.S.R.; validation, S.K., R.C.A. and GSR; formal analysis, S.K., R.C.A. and G.S.R.; investigation, S.K., R.C.A. and G.S.R.; writing—original draft preparation, S.K., R.C.A. and G.S.R.; writing—review and editing, G.S.R.; visualization, S.K. and R.C.A.; supervision, G.S.R. All authors have read and agreed to the published version of the manuscript.

Funding: This work was supported by the Department of Science & Technology (DST-FIST/197/2018-19/580) and the Science & Engineering Research Board (CRG/2021/006513), Government of India.

Data Availability Statement: Not applicable.

Acknowledgments: G.S.R. acknowledges the Department of Science & Technology for the FIST grant (DST-FIST/197/2018-19/580) and the Science and Engineering Research Board for the CRG grant (CRG/2021/006513).

Conflicts of Interest: The authors declare no conflict of interest.

References

1. Paasche, H.; Eberle, D. Rapid integration of large airborne geophysical data suites using a fuzzy partitioning cluster algorithm: A tool for geological mapping and mineral exploration targeting. *Explor. Geophys.* **2009**, *40*, 277–287. [CrossRef]
2. Eberle, D.G.; Daudi, E.X.; Muiuane, E.A.; Nyabeze, P.; Pontavida, A.M. Crisp clustering of airborne geophysical data from the Alto Ligonha pegmatite field, northeastern Mozambique, to predict zones of increased rare earth element potential. *J. Afr. Earth Sci.* **2012**, *62*, 26–34. [CrossRef]
3. Eberle, D.G.; Paasche, H. Integrated data analysis for mineral exploration: A case study of clustering satellite imagery, airborne gamma-ray, and regional geochemical data suites. *Geophysics* **2012**, *77*, B167. [CrossRef]

4. Kitzig, M.C.; Kepic, A.; Kieu, D.T. Testing cluster analysis on combined petrophysical and geochemical data for rock mass classification. *Explor. Geophys.* **2017**, *48*, 344–352. [CrossRef]
5. Wang, Y.; Ksienzyk, A.K.; Liu, M.; Brönner, M. Multigeophysical data integration using cluster analysis: Assisting geological mapping in Trøndelag, Mid-Norway. *Geophys. J. Int.* **2021**, *225*, 1142–1157. [CrossRef]
6. Carranza, E.J.M. Weights of evidence modeling of mineral potential: A case study using small number of prospects, Abra, Philippines. *Nat. Resour. Res.* **2004**, *13*, 173–187. [CrossRef]
7. Porwal, A.; Gonzalez-Alvarez, I.; Markwitz, V.; McCuaig, T.C.; Mamuse, A. Weights-of-evidence and logistic regression modeling of magmatic nickel sulfide prospectivity in the Yilgarn Craton, Western Australia. *Ore Geol. Rev.* **2010**, *38*, 184–196. [CrossRef]
8. Rabeau, O.; Legault, M.; Cheilletz, A.; Jébrak, M.; Royer, J.J.; Cheng, L.Z. Gold potential of a hidden Archean fault zone: The case of the Cadillac–Larder Lake Fault. *Explor. Min. Geol.* **2010**, *19*, 99–116. [CrossRef]
9. Zeghouane, H.; Allek, K.; Kesraoui, M. GIS-based weights of evidence modeling applied to mineral prospectivity mapping of Sn-W and rare metals in Laouni area, Central Hoggar, Algeria. *Arab. J. Geosci.* **2016**, *9*, 373. [CrossRef]
10. Behera, S.; Panigrahi, M.K. Gold prospectivity mapping and exploration targeting in Hutti-Maski schist belt, India: Synergistic application of Weights-of-Evidence (WOE), Fuzzy Logic (FL) and hybrid (WOE-FL) models. *J. Geochem. Explor.* **2022**, *235*, 106963. [CrossRef]
11. Fan, D.; Cui, X.M.; Yuan, D.B.; Wang, J.; Yang, J.; Wang, S. Weight of evidence method and its applications and development. *Procedia Environ. Sci.* **2011**, *11*, 1412–1418. [CrossRef]
12. Harris, J.R.; Grunsky, E.C. Predictive lithological mapping of Canada's North using Random Forest classification applied to geophysical and geochemical data. *Comput. Geosci.* **2015**, *80*, 9–25. [CrossRef]
13. Bhattacharya, S.; Carr, T.R.; Pal, M. Comparison of supervised and unsupervised approaches for mudstone lithofacies classification: Case studies from the Bakken and Mahantango-Marcellus Shale, USA. *J. Nat. Gas Sci. Eng.* **2016**, *33*, 1119–1133. [CrossRef]
14. Masoumi, F.; Eslamkish, T.; Abkar, A.A.; Honarmand, M.; Harris, J.R. Integration of spectral, thermal, and textural features of ASTER data using random forests classification for lithological mapping. *J. Afr. Earth Sci.* **2017**, *129*, 445–457. [CrossRef]
15. Elbegue, A.A.; Allek, K.; Zeghouane, H. Geological mapping using extreme gradient boosting and the deep neural networks: Application to silet area, central Hoggar, Algeria. *Acta Geophys.* **2022**, *70*, 1581–1599. [CrossRef]
16. Shebl, A.; Kusky, T.; Csámer, Á. Advanced land imager superiority in lithological classification utilizing machine learning algorithms. *Arab. J. Geosci.* **2022**, *15*, 923. [CrossRef]
17. Xu, Y.; Zuo, R. Geochemical survey data cube: A useful tool for lithological classification and geochemical anomaly identification. *Geochemistry* **2023**, 125959. [CrossRef]
18. Kaufman, L.; Rousseeuw, P.J. *Finding Groups in Data: An Introduction to Cluster Analysis*; John Wiley & Sons: Hoboken, NJ, USA, 1990. [CrossRef]
19. Bezdek, J.C.; Ehrlich, R.; Full, W. FCM: The fuzzy c-means clustering algorithm. *Comput. Geosci.* **1984**, *10*, 191–203. [CrossRef]
20. Pires, A.C.B.; Harthill, N. Statistical analysis of airborne gammaray data for geologic mapping purposes: Crixas-Itapaci area, Goiás, Brazil. *Geophysics* **1989**, *54*, 1326–1332. [CrossRef]
21. Eberle, D. Geologic mapping based upon multivariate statistical analysis of airborne geophysical data: International Institute for AerospaceSurvey and Earth Sciences. *ITC J.* **1993**, *1993–2*, 173–178.
22. Vulkan, U.; Duval, J.S. Multivariate statistical analysis of geophysical data in Nevada. *Geophysics* **1993**, *58*, 749–755. [CrossRef]
23. Anderson-Mayes, A.M. Strategies to improve information extraction from multivariate geophysical data suites. *Explor. Geophys.* **2002**, *33*, 57–64. [CrossRef]
24. Schetselaar, E.M. Petrogenetic interpretation from gamma-ray spectrometry and geological data: The Arch Lake zoned peraluminous granite intrusion, Western Canadian Shield. *Explor. Geophys.* **2002**, *33*, 35–43. [CrossRef]
25. Martelet, G.; Truffert, C.; Tourlière, B.; Ledru, P.; Perrin, J. Classifying airborne radiometry data with agglomerative hierarchical clustering: A tool for geological mapping in context of rainforest (French Guiana). *Int. J. Appl. Earth Obs. Geoinf.* **2006**, *8*, 208–223. [CrossRef]
26. Eberle, D.; Hutchins, D.; Das, S.; Majumdar, A.; Paasche, H. Automated pattern recognition to support geological mapping and exploration target generation–A case study from southern Namibia. *J. Afr. Earth Sci.* **2015**, *106*, 60–74. [CrossRef]
27. Paasche, H.; Tronicke, J.; Holliger, K.; Green, A.G.; Maurer, H. Integration of diverse physical-property models: Subsurface zonation and petrophysical parameter estimation based on fuzzy c-means cluster analyses. *Geophysics* **2006**, *71*, H33–H44. [CrossRef]
28. Dekkers, M.J.; Heslop, D.; Herrero-Bervera, E.; Acton, G.; Krasa, D. Insight into magmatic processes and hydrothermal alteration of in situ superfast spreading ocean crust at ODP/IODP site 1256 from a cluster analysis of rock magnetic properties. *Geochem. Geophys. Geosyst.* **2014**, *15*, 3430–3447. [CrossRef]
29. Wu, G.; Chen, G.; Cheng, Q.; Zhang, Z.; Yang, J. Unsupervised machine learning for lithological mapping using geochemical data in covered areas of Jining, China. *Nat. Resour. Res.* **2021**, *30*, 1053–1068. [CrossRef]
30. Nivlet, P.; Fournier, F.; Royer, J.J. A new nonparametric discriminant analysis algorithm accounting for bounded data errors. *Math. Geol.* **2002**, *34*, 223–246. [CrossRef]
31. McCammon, R.B.; Botbol, J.M.; Sinding-Larsen, R.; Bowen, R.W. Characteristic analysis-1981: Final program and a possible discovery. *Int. Assoc. Math. Geol.* **1983**, *15*, 59–83. [CrossRef]

32. Botbol, J.M.; Sinding-Larsen, R.; McCammon, R.B.; Gott, G.B. Weighted characteristic analysis of spatially dependent mineral deposit data. *J. Int. Assoc. Math. Geol.* **1977**, *9*, 309–311. [CrossRef]
33. Botbol, J.M.; Sinding-Larsen, R.; McCammon, R.B.; Gott, C.B. A regionalized multivariate approach to target selection in geochemical exploration. *Econ. Geol.* **1978**, *73*, 534–546. [CrossRef]
34. Sandjivy, L. The factorial kriging analysis of regionalized data. Its application to geochemical prospecting. In *Geostatistics for Natural Resources Characterization*; Verly, G., Michel, D., Andre, G., Marechal, A., Eds.; Reidel Publishing Company: Dordrecht, Netherlands, 1984; Volume 122, pp. 559–571. [CrossRef]
35. Royer, J.J. Proximity analysis: A method for multivariate geodata processing. Application to geochemical processing. *Sci. La Terre Série Inform.* **1984**, *20*, 223–243.
36. Chaudhuri, B.K.; Roy, R.K. Gold mineralization in Eastern India-Status Review and a Look to the Future. *Geol. Surv. India Spec. Publ.* **2001**, *58*, 29–57.
37. Saha, A.K. Crustal evolution of Singhbhum North Orissa, Eastern India. *Mem. Geol. Surv. India* **1994**, *27*, 341.
38. Dey, S.; Topno, A.; Liu, Y.; Zong, K. Generation and evolution of Paleoarchean continental crust in the central part of the Singhbhum craton, eastern India. *Precambrian Res.* **2017**, *298*, 268–291. [CrossRef]
39. Singh, S.; Chakravarti, R.; Barla, A.; Behera, R.C.; Neogi, S. A holistic approach on the gold metallogeny of the Singhbhum crustal province: Implications from tectono-metamorphic events during the Archean-Proterozoic regime. *Precambrian Res.* **2021**, *365*, 106376. [CrossRef]
40. Arasada, R.C.; Srinivasa Rao, G.; Anand, R. Crustal architecture of North Singhbhum Mobile Belt, Eastern Indian Shield: Constraints from two-dimensional and three-dimensional modelling of Bouguer gravity and aeromagnetic data. *Geol. J.* **2022**, *57*, 2668–2685. [CrossRef]
41. Sanyal, S.; Sengupta, P. Metamorphic evolution of the Chotanagpur granite gneiss complex of the east Indian shield: Current status. *Geol. Soc. Spec. Publ.* **2012**, *365*, 117–145. [CrossRef]
42. Mukherjee, S.; Dey, A.; Sanyal, S.; Ibanez-Mejia, M.; Dutta, U.; Sengupta, P. Petrology and U-Pb geochronology of zircon in a suite of charnockitic gneisses from parts of the Chotanagpur Granite Gneiss Complex (CGGC): Evidence for the reworking of a Mesoproterozoic basement during the formation of the Rodinia supercontinent. In *Crustal Evolution of India and Antarctica: The Supercontinent Connection*; Pant, N.C., Dasgupta, S., Eds.; Special Publications; Geological Society: London, UK, 2017; Volume 457, pp. 197–232. [CrossRef]
43. Mazumder, R. Proterozoic sedimentation and volcanism in the Singhbhum crustal province, India and their implications. *Sediment. Geol.* **2005**, *176*, 167–193. [CrossRef]
44. Mazumder, R.; De, S.; Ohta, T.; Flannery, D.; Mallik, L.; Chaudhury, T.; Chatterjee, P.; Ranaivoson, M.A.; Arima, M. Chapter 10 Palaeo-Mesoproterozoic sedimentation and tectonics of the Singhbhum Craton, eastern India, and implications for global and craton-specific geological events. *Geol. Soc. Lond. Mem.* **2015**, *43*, 139–149. [CrossRef]
45. De, S.; Mallik, L.; Mazumder, R.; Chatterjee, P.; Ohta, T.; Saito, S.; Chiarenzelli, J. Sedimentation history of the Paleoproterozoic Singhbhum Group of rocks, eastern India and its implications. *Earth Sci. Rev.* **2016**, *163*, 141–161. [CrossRef]
46. Olierook, H.K.; Clark, C.; Reddy, S.M.; Mazumder, R.; Jourdan, F.; Evans, N.J. Evolution of the Singhbhum Craton and supracrustal provinces from age, isotopic and chemical constraints. *Earth-Sci. Rev.* **2019**, *193*, 237–259. [CrossRef]
47. Sesha Sai, V.V. *A Report on Exploration for Gold in Babaikundi-Birgaon Sector, District Ranchi, Bihar*; Geological Survey of India: Ranchi, India, 1998; unpublished work.
48. Madhusudan, I.C.; Maiti, S.K.; De, M.K.; Singh, A.; Das, P.C. Geophysical Studies of Tamar Gold Prospect, Babaikundi-Birgaon Sector, District Ranchi. Bihar. *Indian Miner.* **1999**, *53*, 37–44.
49. Sharan, R.R.; Kurien, P.S. *Final Report on Investigation for Gold in Parts of Sonapet Valley, Paschimi Singhbhum and Ranchi Districts*; Geological Survey of India: Ranchi, India, 2004; unpublished work.
50. Jha, V.; Singh, S.; Venkatesh, A.S. Invisible gold occurrence within the quartz reef pyrite of Babaikundi area, North Singhbhum fold-and-thrust belt, Eastern Indian Shield: Evidence from petrographic, SEM and EPMA studies. *Ore Geol. Rev.* **2015**, *65*, 426–432. [CrossRef]
51. Horo, D.; Pal, S.K.; Singh, S.; Srivastava, S. Combined self-potential, electrical resistivity tomography and induced polarisation for mapping of gold prospective zones over a part of Babaikundi-Birgaon Axis, North Singhbhum Mobile Belt, India. *Explor. Geophys.* **2020**, *51*, 507–522. [CrossRef]
52. Majumdar, S.; Singh, S.; Sahoo, P.R.; Venkatesh, A.S. Trace element systematics of pyrite and its implications for refractory gold mineralization within the carbonaceous metasedimentary units of Paleoproterozoic South Purulia Shear Zone, eastern India. *J. Earth Syst. Sci.* **2019**, *128*, 233. [CrossRef]
53. Barla, A.; Singh, S.; Chakravarti, R. Genesis of metasomatic gold mineralization in the Pahardiha-Rungikocha gold deposits, eastern India: Constraints from trace elements signatures in chromite-cored magnetite and bulk geochemistry. *Ore Geol. Rev.* **2020**, *121*, 103482. [CrossRef]
54. Chakravarti, R. Genesis of Gold Mineralization Associated with Archean Quartzpebble-Conglomerates (QPC) in and Around the Eastern Iron Ore Group, Singhbhum Craton, Eastern India. Ph.D. Thesis, Indian Institute of Technology (Indian School of Mines), Dhanbad, India, 2020.
55. GSI. *Catalogue of Aero-Geophysical Maps*; Airborne Mineral Surreys and Exploration Wing: Bangalore, India, 1995.

56. Keating, P.; Pinet, N.; Pilkington, M. Comparison of some commonly used regional residual separation techniques. In *International Workshop on Gravity, Electrical & Magnetic Methods and Their Applications*; Society of Exploration Geophysicists: Beijing, China, 2011; p. 14.
57. Zheng, A.; Casari, A. *Feature Engineering for Machine Learning: Principles and Techniques for Data Scientists*; O'Reilly Media: Sebastopol, CA, USA, 2018; p. 218.
58. Novàk, V.; Perfilieva, I.; Mockor, J. *Mathematical Principles of Fuzzy Logic*; Kluwer Academic Publishers: Alphen am Rhein, The Netherlands, 1999; p. 320.
59. Eldosouky, A.M.; Pham, L.T.; Duong, V.H.; Kemgang Ghomsi, F.E.; Henaish, A. Structural interpretation of potential field data using the enhancement techniques: A case study. *Geocarto Int.* **2022**, *37*, 16900–16925. [CrossRef]
60. Pham, L.T.; Oksum, E.; Kafadar, O.; Trinh, P.T.; Nguyen, D.V.; Vo, Q.T.; Le, S.T.; Do, T.D. Determination of subsurface lineaments in the Hoang Sa islands using enhanced methods of gravity total horizontal gradient. *Vietnam J. Earth Sci.* **2022**, *44*, 395–409.
61. Thorndike, R.L. Who belongs in the family? *Psychometrika* **1953**, *18*, 267–276. [CrossRef]
62. Caliński, T.; Harabasz, J. A dendrite method for cluster analysis. *Commun. Stat.-Theory Methods* **1974**, *3*, 1–27. [CrossRef]
63. Rousseeuw, P.J. Silhouettes: A graphical aid to the interpretation and validation of cluster analysis. *Comput. Appl. Math.* **1987**, *20*, 53–65. [CrossRef]